THERMODYNAMIC STUDY OF MOLTEN POOL DURING SELECTIVE LASER MELTING OF ALSI10MG ALLOY

Xiaonan NI [1], Ansen WANG [1], Zijian HU [1], Wenxin YANG [1], Zhenjie HU [1], Yongkang LUO [1], Zhe ZHAO [1,*], Xin DENG [1,*], Hongwei WANG [2], Zhi QU [3,4], Feng JIN [3,4], Li HE [3,4]

1. School of Electromechanical Engineering, Guangdong University of Technology, Guangzhou 510006, China

2. Guangzhou Riton Additive Technology Co., Ltd., Guangzhou 510387, China

3. Guangdong Metal Ceramic 3D Technology Co., Ltd., Foshan 528225, China

4. Guangdong Fenghua Zhuoli Technology Co., Ltd., Foshan 528200, China

[*] Corresponding author; E-mail: zhezhao@gdut.edu.cn ; dengxin@gdut.edu.cn

A study of the thermodynamic behavior during the Selective Laser Melting process of AlSi10Mg alloy was conducted using a combined numerical simulation and experimental approach. A multiphase flow model incorporating gas-liquid-solid phases was established. The numerical simulation results aligned well with experimental findings, affirming the reliability of the numerical model. Insufficient and excessive laser power densities respectively led to incomplete fusion defects and spherical pore defects. The evolution of the melt pool was primarily influenced by recoil pressure, Marangoni force, and surface tension, resulting in keyhole formation, convective flow, and liquid surface oscillation as characteristic features of melt pool evolution. Solidification process and mechanical analyses revealed that the central region of the melt pool exhibited smaller temperature gradients and higher solidification rates. Properly increasing the scanning speed under suitable laser power conditions is more conducive to optimizing the solidification structure and enhancing the mechanical properties of SLM components. This study elucidates the thermodynamic evolution mechanism during the SLM process of aluminum-based alloys, providing theoretical support and guidance for optimizing the SLM process.

Key words: *Selective laser melting; Thermodynamic behavior; Pore defects; Molten pool driving force; Solidification mechanism*

1. Introduction

Additive manufacturing (AM), or 3D printing, is a rapid prototyping technology that constructs objects by sequentially depositing powdered metal or plastic layers based on digital models [1]. This process typically utilizes material printers based on digital technologies, enabling the direct fabrication of complex structural products. Compared to subtractive manufacturing, additive manufacturing offers significant advantages such as greater design freedom and higher efficiency, making it widely

applicable in fields such as medicine, aerospace, and automotive industries [2,3]. The direct and precise shaping characteristics of additive manufacturing not only drive the development of complex structures but also promote the transformation of material systems and processing technologies.

Laser Additive Manufacturing (LAM) is a technique that uses a laser heat source to rapidly melt and solidify powdered materials, followed by layer-by-layer deposition to form objects, belonging to a category of 3D printing processes [4]. For metal materials, LAM mainly includes Selective Laser Melting (SLM) and Direct Energy Deposition (DED) technologies [5]. SLM technology uses a high-energy laser beam to melt a layer of metal powder, which then solidifies to form a three-dimensional solid part [6]. On the other hand, DED technology directly generates a molten pool in the deposition area under the action of a laser, and then feeds the material as powder or wire directly into the high-temperature melt pool, mainly used in the preparation of large-sized metal components [7]. SLM technology achieves melting and solidification by first depositing powder and then laser scanning, with the static nature of the powder resulting in higher forming accuracy, suitable for additive manufacturing of small-sized parts.

The SLM process involves complex physical phenomena such as heat transfer, material phase changes, and interfacial interactions [8]. During the SLM process, frequent heating and cooling cycles can lead to significant temperature gradients and unstable melt pools. The temperature history and melt pool evolution process directly affect the microstructure and ultimately determine the mechanical properties. Therefore, under certain processing conditions, additive manufacturing still faces some limitations, such as issues with cracks and pore defects. Among them, pore defects have the most significant impact on mechanical properties, and these pores are difficult to eliminate completely even through heat treatment [9]. Pore defects are usually accompanied by melt pool movement, making an in-depth exploration of the melt pool evolution mechanism of great significance. Parameters such as laser power and scanning speed directly affect the geometry of the melt pool, and changes in driving force distribution under different process parameters, including gasification recoil pressure, Marangoni force, and surface tension, also occur [10,11]. Gasification recoil pressure and Marangoni force can cause varying degrees of depression on the liquid surface of the melt pool, resulting in a keyhole shape, while Marangoni force can enhance heat transfer in the melt pool [12]. Regarding surface tension, a smooth melt pool surface can be obtained when the molten metal is well-bonded to the substrate, whereas poor wetting and an unstable melt pool can lead to the splitting of the melt pool into single or multiple spherical regions, resulting in a balling effect [13]. Zuo et al. [14] conducted numerical simulations based on the finite element method and found that surface tension and gasification recoil pressure jointly influence the melt pool morphology, with surface tension having a greater impact on the melt pool morphology when the temperature peak is below the material's boiling point. Weirather et al. [15] used the Smoothed Particle Hydrodynamics (SPH) method for SLM numerical simulations and observed the evolution process of the melt pool shape. Liu et al. [16] conducted a multi-layer multi-pass simulation study, which showed that with the increase in layers, the peak temperature, geometric size, and existence time of the melt pool all increased. Scharowsky et al. [17] captured images of melt pool morphology during electron beam melting and observed the evolution process of the melt pool, noting periodic oscillations of the liquid surface for the first time. Bruna-Rosso et al. [18] through numerical simulations combined with experiments, observed changes in melt pool size and insufficient melting of metal powder, among other defects.

In conclusion, existing studies have explored the effects of process parameters on melt pool morphology, but there are few reports on the relationship between melt pool evolution characteristics and thermodynamic parameters, especially the quantitative relationship between driving forces and melt pool geometric characteristics, and the thermodynamic mechanisms remain unclear. Therefore, this study uses a numerical model that unifies the gas-liquid-solid phases to solve the melt pool evolution process during the SLM process, combined with experimental results, to analyze in-depth the inherent relationship between process parameters, melt pool evolution laws, and component performance.

2. Selective laser melting experiment

This study utilized AlSi10Mg alloy powder with particle morphology approximately spherical, and a median particle size of 30 μm. The experiments were conducted on an SLM-100C device equipped with a German IPG 1000 W single-mode fiber laser with a wavelength of 1064 nm. Argon gas was used as the circulating protective gas in the printing chamber, and the laser beam scanning path was in a checkerboard pattern, with a inter-layer offset angle of 67°. The selective laser melting (SLM) process is depicted in Fig. 1, including model input, control system, optical path transmission system, and forming system. During the SLM process, the powder layer thickness was 0.03 mm, the scan spacing was 0.06 mm, the laser power is 300 W, and the scan speed increased from 900 mm/s to 2400 mm/s.

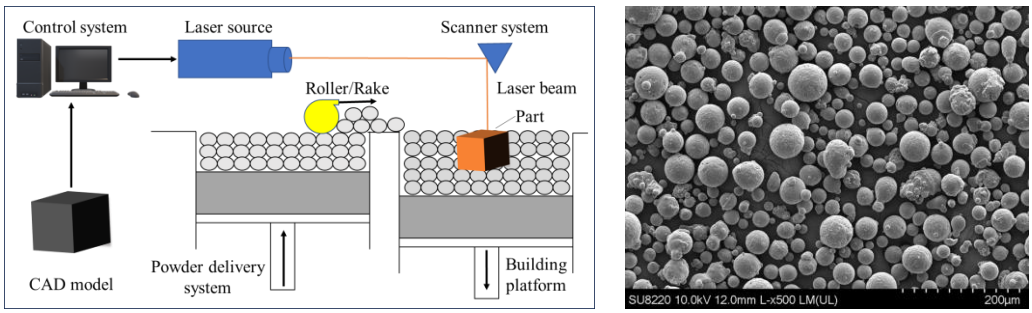

(a) **(b)**

Fig. 1. (a) Selective laser melting forming system, (b) Powder morphology of AlSi10Mg.

3. Physical and mathematical models

3.1. Model assumption

The SLM process involves complex interactions among multiple physical fields, as depicted in Fig. 2, encompassing physical phenomena such as melting, vaporization, and solidification of metal particles. Following laser irradiation of the powder bed, metal particles are either reflected or absorbed, undergoing heat conduction between particles and the substrate to form a melt pool, which subsequently cools and solidifies to create a melt track. It is noteworthy that the aforementioned physical phenomena interact with one another. Melt pool flow enhances heat transfer, while temperature distribution reciprocally influences melt pool flow; the vaporization of metal melt accelerates heat dissipation, and the recoil pressure resulting from vaporization further impacts melt pool evolution.

The highly nonlinear thermal properties of metal materials significantly increase the computational workload. To balance computational efficiency and accuracy, this study made the following assumptions about the computational model [19]: (1) Metal powder is considered an opaque medium, and reflections between powder particles are disregarded. (2) Metal powder is assumed to be isotropic, with its physical properties being temperature-dependent. (3) The liquid metal and gas are treated as incompressible Newtonian fluids with laminar characteristics. (4) The mushy zone between the solid phase and liquid phase is treated as an isotropic porous medium. (5) The buoyancy term caused by temperature changes is calculated using the Boussinesq approximation.

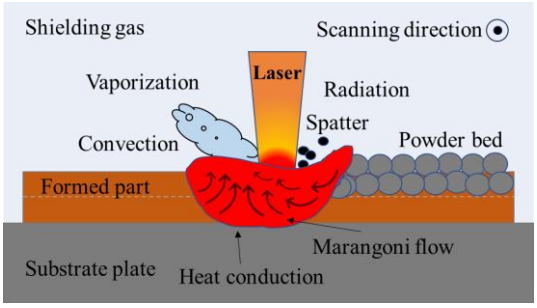

Fig. 2. Complex physical phenomena in SLM forming process.

3.2. The heat-fluid governing equation

This study is based on the numerical solution of the Navier-Stokes equations, which include the continuity equation, the momentum conservation equation, and the energy conservation equation, as shown in equations (1)-(3):

$$\nabla \cdot \vec{u} = 0 \tag{1}$$

$$\rho \frac{\partial \vec{u}}{\partial t} + \rho(\vec{u} \cdot \nabla)\vec{u} = -\nabla p + \mu \nabla^2 \vec{u} - \rho \vec{g} + \rho \vec{g} \beta \left(T - T_{\mathrm{m}}\right) + F_{Darcy} + F_{vol} \tag{2}$$

$$\rho C_p^{cq} \left[\frac{\partial T}{\partial t} + \vec{u} \cdot \nabla(T) \right] = \nabla(k \nabla T) + Q_{laser} \delta(\phi) - Q_{loss} \tag{3}$$

In equation (1), ∇ is the gradient operator, and and $\vec{u}$ is the velocity vector. In equation (2), ρ, t, P, μ, $\vec{g}$ are density, time, pressure, dynamic viscosity and gravity vector, respectively. β is the thermal expansion coefficient, T is the temperature, and T_{m} is the melting temperature. In equation (3), C_p^{cq} is equivalent specific heat capacity, k is the thermal conductivity, Q_{laser} is the input heat of the laser, and Q_{loss} is the heat loss.

F_{Darcy} in equation (2) is Darcy damping force, whose function is to solve the momentum loss caused by material melting and solidification [20]. F_{vol} stands for momentum source term, including surface tension, Marangoni force, and gasification recoil pressure, which together control the flow of metal powder after melting. The specific expression is as follows:

$$F_{Darcy} = -Kc \frac{\left(1 - g_l\right)^2}{\left(g_l^3 + B\right)} \vec{u} \tag{4}$$

Where, K_c and B are constants that inhibit the velocity of the mushy zone, and their values are 1E6 and 1E-3, respectively; g_l is the volume fraction of the liquid metal, and g_l decreases to 0 when the mushy zone is completely solidified, and Darcy resistance reaches its maximum.

$$F_{vol} = \sigma\kappa\vec{n}\delta(\phi) + \left[\vec{\nabla}T - \vec{n}(\vec{\nabla}T \cdot \vec{n})\right]\frac{d\sigma}{dT} + P_{recoil}\vec{n}\delta(\phi) \tag{5}$$

Where σ is the surface tension, κ (1/m) is the surface curvature of the molten pool, $\vec{n}$ is the normal vector of the surface, and $\delta(\phi)$ converts the surface force into the volume force as the source term of the momentum equation. The laser heat source is a surface heat source in the form of Gaussian distribution [21], and the expression is as follows:

$$Q_{laser} = \frac{2AP_{laser}}{\pi r_0^2}\exp\left(\frac{-2r_1^2}{r_0^2}\right)\delta(\phi) \tag{6}$$

Where, A is the laser absorption rate, P_{laser} is the laser power, r_0 is the laser spot radius, and r_1 is the radial distance from a certain point on the surface of the material to the center of the laser spot.

The Q_{loss} in equation (3) is the source term of heat source loss, which includes convective heat loss, radiant heat loss and vaporization heat loss. The expression is as follows:

$$Q_{loss} = \left\{h_c\left(T - T_0\right) + \sigma_r k_b\left(T^4 - T_0^4\right) + L_v\dot{m}\right\}\delta(\phi) \tag{7}$$

Where, h_c is the convective heat transfer coefficientl, σ_r is the surface emissivity of the material, L_v is the latent heat of vaporization, $\dot{m}$ is the vaporization rate, and $\delta(\phi)$ is the phase field function that controls the heat loss only at the gas-liquid interface [22].

3.3. Physical property and calculation Settings

The physical properties of the material in the numerical simulation were set according to the AlSi10Mg and Argon, as shown in Table 1.

Table 1. Thermal properties of AlSi10Mg and Argon [23]**.**

Parameter	Symbol	AlSi10Mg	Argon
Density (kg/m^3)	ρ	2680 (*s, l*)	1.6337 (*g*)
Thermal conductivity (W/m·k)	k	238 (*s*), 100 (*l*)	0.0177 (*g*)
Specific heat (J/kg·k)	C_p	917 (*s*), 1080 (*l*)	520 (*g*)
Thermal expansion coefficient (k^{-1})	β	1×10^{-6} (*l*)	3.41×10^{-3} (*g*)
Dynamic viscosity (kg/m·s)	μ	1.2×10^{-3} (*l*)	2.25×10^{-5} (*g*)
Surface tension (N/m)	σ	1.2 (*l*)	
Solidus temperature (K)	T_s	830.15	
Liquids temperature (K)	T_l	893	
Evaporating temperature (K)	T_v	2338	
Latent heat of fusion (J/kg)	L_f	3.54×10^5	
Enthalpy change of vaporization (J/kg)	L_v	1.05×10^7	
Temperature coefficient of surface tension (N/m·k)	$\frac{d\sigma}{dT}$	-3×10^{-4}	

(*s*, *l* and *g* are solid, liquid and gas, respectively).

Considering the computational expenses, this research employs a two-dimensional computational domain for numerical simulation. The transition from three dimensions to two

dimensions is illustrated in Fig. 3 (a) and (b). The movement of the laser heat source is modeled as the beam traversing a two-dimensional cross-section of the powder bed, with its temporal evolution described by a Gaussian pulse function.

The two-dimensional computational domain, depicted in Fig. 3 (b), comprises powder particles of approximately spherical shape with a median particle diameter of 30 μm uniformly dispersed on the substrate. The walls of the metal domain are assumed to exhibit a heat flux boundary condition, while the boundaries of the gas domain are set as pressure outlet boundaries at 1 atm. The initial temperature is set at 300 K, with the bottom wall treated as an adiabatic boundary condition. The mesh division type is free tetrahedral mesh. Furthermore, the vicinity of the powder particles undergoes mesh refinement to capture the intricate flow details of the melt pool, as shown in Fig. 3 (c). In addition, in order to avoid the influence of the grid on the simulation results, the grid independence is tested based on the change of the molten pool area over time. As shown in Fig. 3 (d), the number of mesh units corresponding to mesh-01, mesh-02 and mesh-03 is 36170, 47378 and 56606 respectively, and the variation of the melt pool area corresponding to mesh-02 and mesh-03 is basically the same. Therefore, this study carried out numerical simulation based on mesh-03.

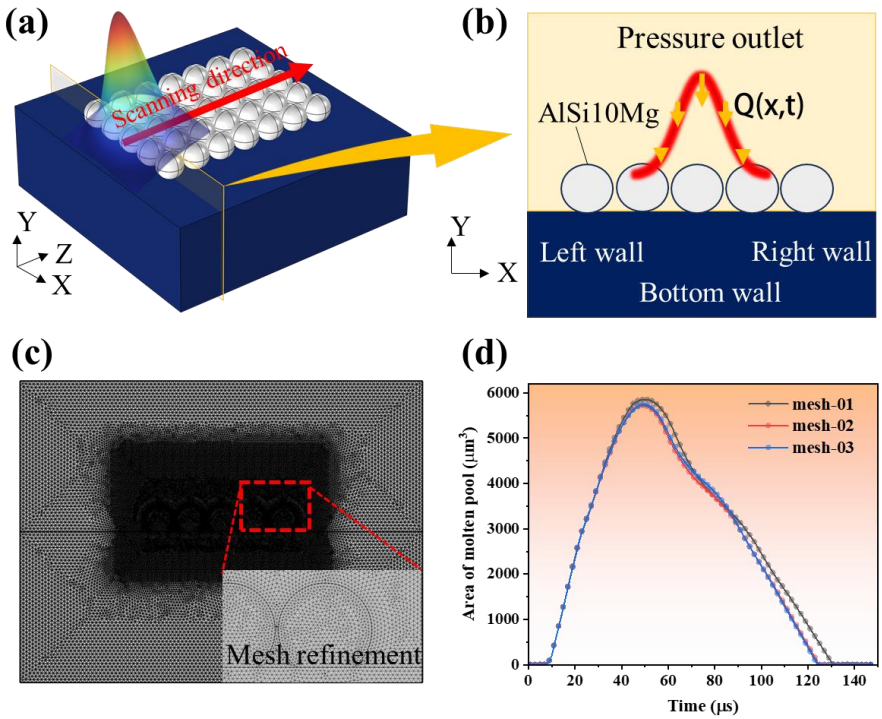

Fig. 3. (a) Three-dimensional computing domain, (b) Two-dimensional computing domain and boundary conditions, (c) Mesh and local refinement, (d) Grid grid independent test.

4. Results and discussion

4.1. Molten pool defects and model validation

Fig. 4(a)-(f) depict optical micrographs of sample cross-sections at different scanning speeds when the laser power is 300 W. At scanning speeds of 900 mm/s and 1200 mm/s, the higher energy density at lower scanning speeds leads to significant gasification recoil pressure, resulting in more keyhole pores. Additionally, gases generated by local material vaporization may remain in the melt

pool, forming residual bubbles. The number of pores is relatively low at scanning speeds of 1500 mm/s and 1800 mm/s. At 2100 mm/s, some non-spherical pores begin to appear, and the pore area significantly increases at 2400 mm/s. Non-spherical pore defects are mainly due to insufficient energy at high scanning speeds, resulting in incomplete melting of the powder and the formation of incompletely fused pores, most of which are located at the edge of the melt pool. Fig. 4(g) shows the relative density of the samples measured using the Archimedean drainage method. The relative density first increases and then decreases with increasing scanning speed, reaching a maximum of 98.3% at 1800 mm/s.

These results indicate that at a laser power of 300 W, lower scanning speeds lead to more spherical pore defects, while higher scanning speeds lead to more pronounced non-spherical pore defects. For AlSi10Mg powder, defect-free and dense SLM components can be obtained at a scanning speed of 1800 mm/s.

After the cross-section of the AlSi10Mg sample is corroded with an aluminum alloy corrosion agent, the solidification trajectory of the melt pool can be clearly observed, providing a benchmark for comparing with simulation results. Fig. 5 shows the variation of the melt pool morphology with laser scanning speed, with the numerical value in the bottom left corner indicating the ratio of melt pool width to depth. The width-to-depth ratio of the melt pool increases with increasing scanning speed. At 2400 mm/s, due to insufficient laser energy, the powder cannot be completely melted, resulting in spheroidization under the action of surface tension, as shown by the red dashed line in Fig. 5(c). The numerical simulation results exhibit a similar trend, with an error of less than 5% compared to experimental results, indicating good overall agreement and verifying the accuracy of the computational model for thermodynamic analysis of melt pool evolution.

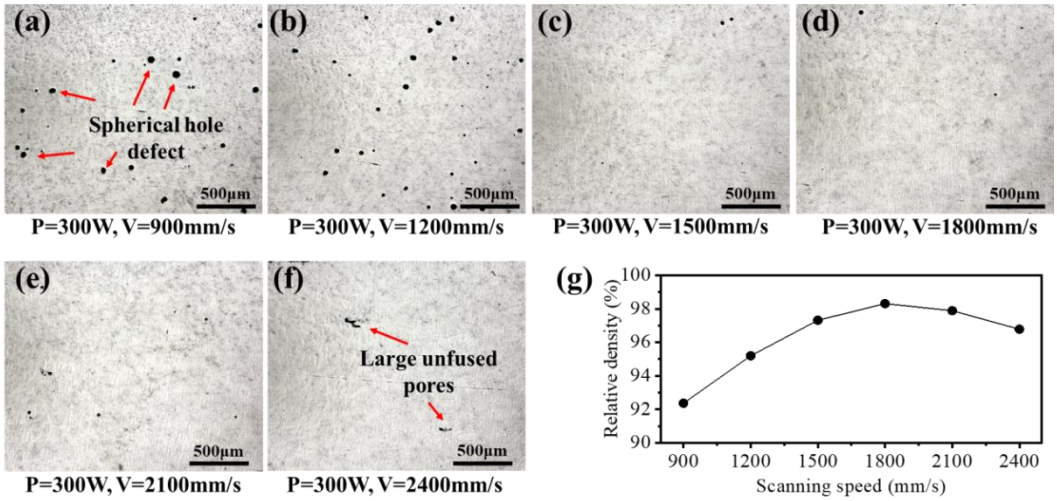

Fig. 4. (a)-(f) Pore defect distribution，(g) Change of relative density with scanning speed.

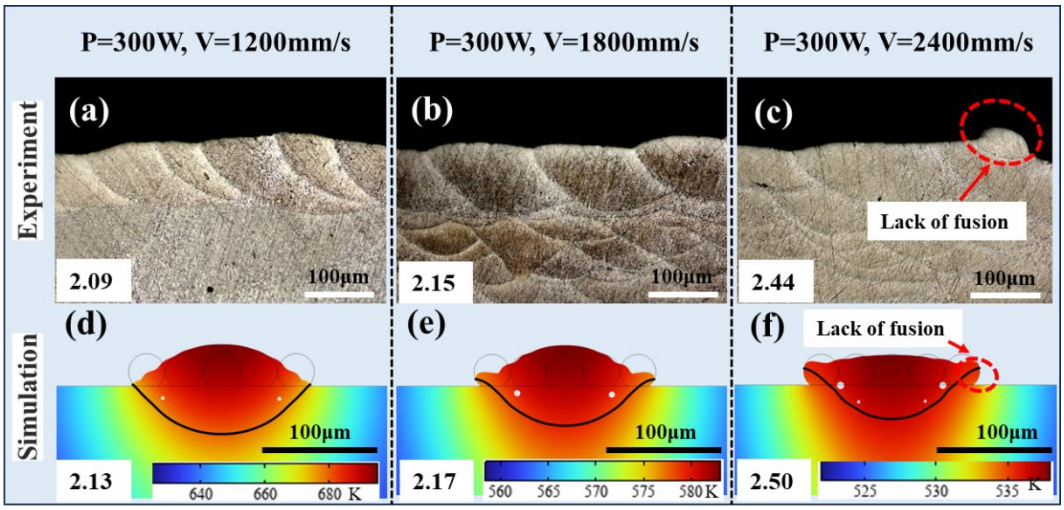

Fig. 5. Comparison of molten pool morphology between numerical simulation and experiment.

4.2. Thermodynamic evolution of molten pool

The convection movement of the melt pool is influenced by viscosity and driven by various external forces (such as gasification recoil pressure, Marangoni force, surface tension, gravity, and buoyancy), especially the first three forces play important roles in the evolution of the melt pool [8]. Fig. 6 shows the evolution process of the melt pool at 300 W and 1800 mm/s. The black solid line represents the contour line of 893 K, which indicates the boundary between the melt pool and the solid, with the metal liquid above and the metal solid below. The black arrows in the figure represent the velocity vectors of the melt pool, and the white approximately spherical region is the ambient gas trapped inside the melt pool.

As the laser heat source moves, the surface of the metal powder begins to melt and collapse, and then the melt pool area gradually increases, as shown in Fig. 6 (b)-(d). When the surface temperature of the melt pool reaches above the vaporization temperature of 2338 K, with the gradual increase of gasification recoil pressure, the melt pool liquid surface starts to deform and sag. At 40 μs, the liquid surface of the melt pool exhibits a significant concave shape. After 50 μs, the melt pool starts to cool gradually, and the liquid surface of the melt pool shows up-and-down oscillations under the action of surface tension until it completely solidifies and becomes stationary.

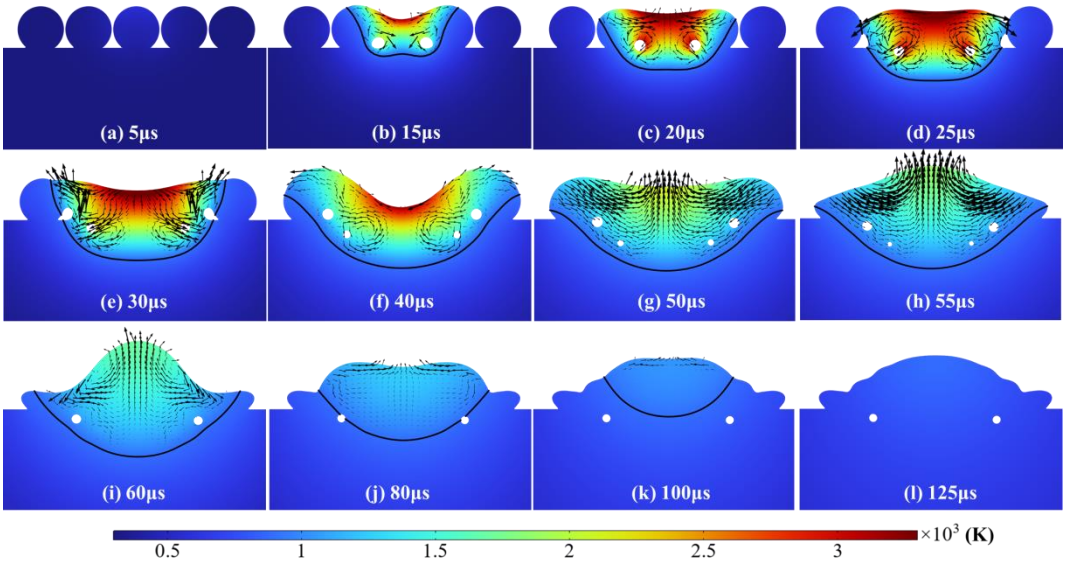

Fig. 6. The molten pool evolution process at 300W-1800mm/s.

Fig. 7 depicts the distribution cloud map of the driving forces acting on the melt pool, which belong to the surface forces of the liquid metal and are mainly distributed at the gas-liquid interface. In the figure, the blue dashed box indicates the time period of the driving force, and the red arrows represent the direction of the driving force. From Fig. 7 (a), it can be seen that the recoil pressure mainly acts near the center of the laser spot, with the force pointing downward into the melt pool. Fig. 7 (b) shows that the Marangoni force mainly acts within half of the melt pool size, with the force direction pointing from the center of the melt pool towards the sides, which is also the main reason for the formation of the Marangoni circulation effect. Fig. 7 (c) demonstrates that surface tension exists almost throughout the entire melt pool interface. It is worth noting that the direction of surface tension is constantly changing, and it varies in magnitude and direction at different positions of the melt pool interface, which is the main cause of the later-stage up-and-down oscillatory motion of the melt pool. Additionally, it is observed that the duration of the three driving forces increases sequentially, with surface tension almost spanning the entire lifecycle of the melt pool and playing a dominant role in the middle and later stages.

The evolution of melt pool morphology is the result of the complex interplay between the laser heat source and various driving forces. Here, we characterize the dynamic evolution of the melt pool by examining the changes in melt pool liquid level over time. Fig. 8 illustrates the variation of the melt pool liquid level with time. During the initial stage of powder melting, the melt pool surface undergoes a minor collapse under the influence of weak recoil pressure and gravity, leading to the formation of the first trough at 15 μs. As the powder continues to melt, the surface tension gradually increases, counterbalancing the recoil pressure and causing the melt pool interface to rise, resulting in the first peak at 25 μs. Subsequently, the recoil pressure increases significantly, reaching its maximum depth at 42 μs, corresponding to the lowest position of the melt pool liquid level. As the laser heat source gradually moves away, the recoil pressure diminishes, the Marangoni force weakens, and the surface tension begins to play a dominant role. Given that the direction of surface tension is perpendicular to the melt pool interface, the melt pool liquid level exhibits up-and-down oscillatory motion due to inertia, as observed in the waveband between 75 μs and 120 μs in Fig. 8. This behavior is akin to the oscillations reported by Scharowsky et al. [17] in electron beam melting. Furthermore, the gasification

recoil pressure only affects the initial stage of the melt pool cycle, the Marangoni force operates in the first half of the melt pool cycle, while surface tension is present throughout almost the entire melt pool cycle. Therefore, surface tension significantly influences the late-stage oscillatory motion of the melt pool, which aligns with the findings presented in Fig. 7 (c).

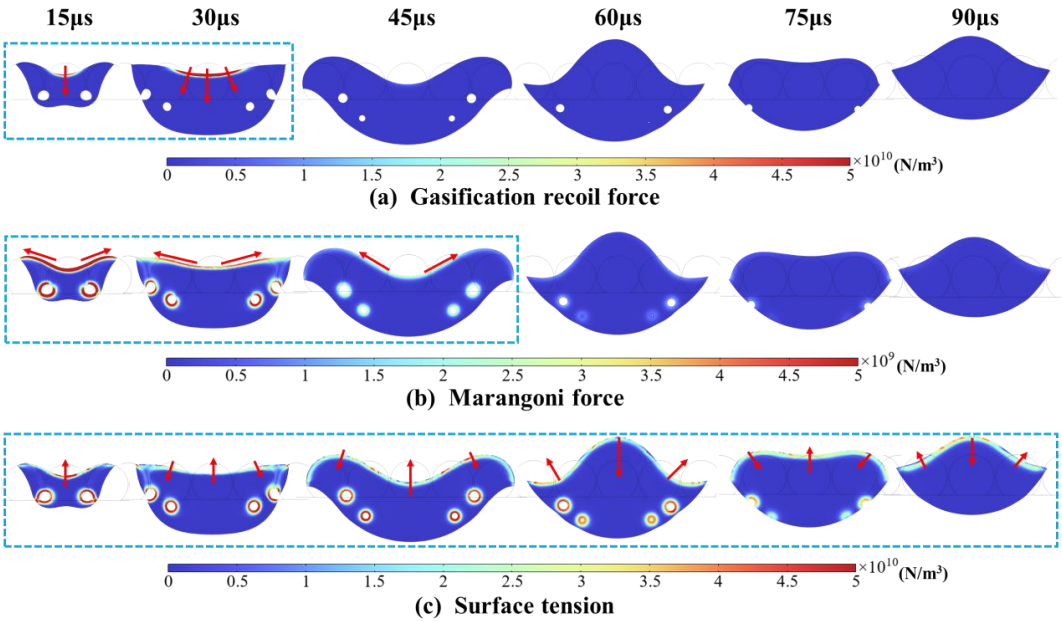

Fig. 7. Distribution of Gasification recoil pressure, Marangoni force and surface tension at the interface of molten pool.

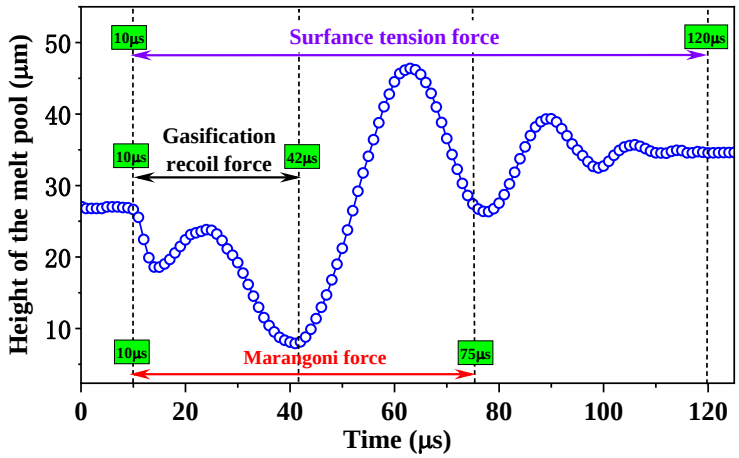

Fig. 8. Change of molten pool level with time.

4.3. Analysis of transient solidification mechanism

The solidification process of molten pool is very rapid, and the transient solidification process controls the morphology of microscopic grains and directly affects the final mechanical properties of formed parts [24]. Temperature gradient G and solidification rate R are the key parameters that determine the solidification structure, and they affect the shape and size of the microscopic grains, respectively. Smaller G and larger R are conducive to the formation of fine microstructure. The formula for calculating G and R is as follows [25] :

$$\mathrm{G}\left(\mathrm{K/m}\right)=\nabla T\cdot\vec{\mathbf{n}} \tag{8}$$

$$\mathrm{R}\left(\mathrm{m/s}\right)=\frac{\text{Cooling rate (K/s)}}{\text{Temperature gradient (K/m)}} \tag{9}$$

Where, $\vec{\mathbf{n}}$ is the unit normal vector at the solid-liquid interface pointing to the interior of the molten pool.

In order to quantitatively analyze the solidification parameters of local regions in the melt pool, monitoring points were set at the center (point 1), edge (point 2), and bottom (point 3) of the melt pool for data extraction, as shown in the insets of Fig. 9 (a) and (b). The variation of G and R over time at different monitoring points indicates that the temperature gradient at points 1, 2, and 3 increases sequentially, while the solidification rate decreases sequentially throughout the entire solidification process. Both G and R show a general decreasing trend but exhibit fluctuations rather than a linear pattern. The fluctuation amplitude is greatest at point 1, which is closer to the melt pool surface, where the fluctuation of the melt pool liquid level leads to more drastic temperature changes.

Fig. 9 (c) and (d) show the distribution maps of G and R, respectively. The maximum value of G at the edge of the melt pool is 1.26 E7 K/m, which is about 7 times higher than the value of 1.78 E6 K/m at the top of the melt pool. The maximum value of R at the top of the melt pool is 8.34 m/s, which is approximately 15 times higher than the value of 0.57 m/s at the edge of the melt pool. The top of the melt pool exhibits a smaller temperature gradient and a larger solidification rate, resulting in a finer microstructure, whereas the opposite is true for the edge and bottom of the melt pool.

It can be inferred from the above analysis that the variation in solidification rate reflects the solidification behavior under certain parameters, thereby predicting the relationship between process parameters and microstructure.

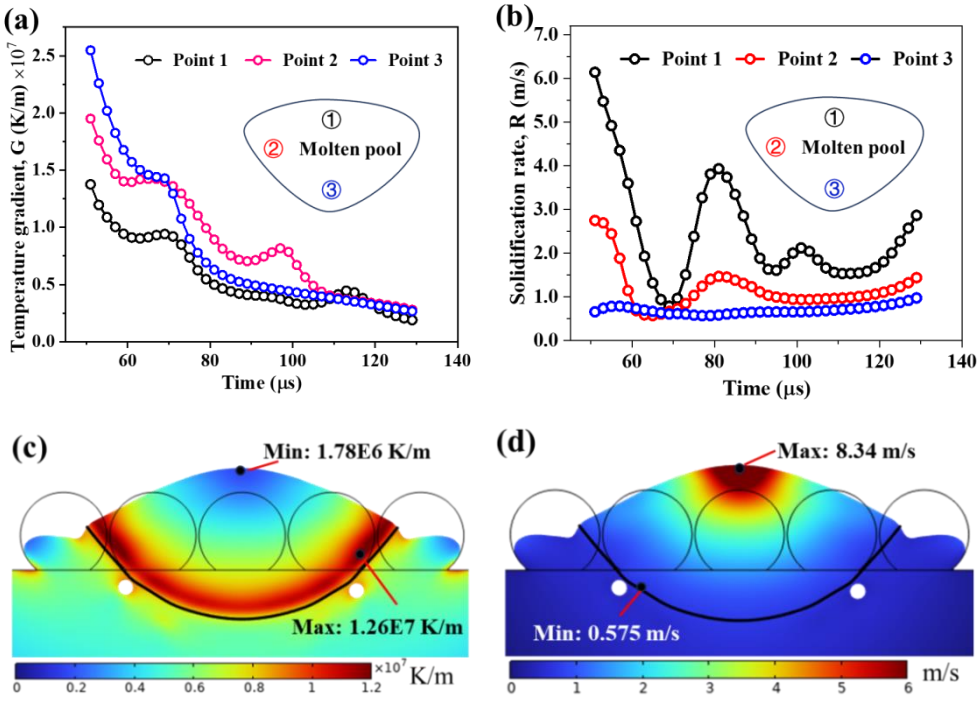

Fig. 9. Solidification process of molten pool. (a) The change of G at the monitoring point, (b) The change of R at the monitoring point, (c) Temperature gradient cloud map, (d) Solidification rate cloud map.

The solidification process of the melt pool is crucial for grain refinement, and a faster cooling rate favors grain refinement [24]. To investigate the relationship between process parameters, cooling rate, and mechanical properties, a comparative study was conducted on the cooling rates and mechanical properties at different scanning speeds under a laser power of 300W.

As shown in Fig. 10(a), with increasing scanning speed, the moment when the melt pool begins to cool advances sequentially, starting at 55 μs, 40 μs, and 30 μs respectively. The higher the scanning speed, the shorter the cooling time of the melt pool. At a scanning speed of 2400 mm/s, the cooling time of the melt pool (30 μs - 100 μs) is significantly shortened, with the maximum cooling rate reaching 3.49 E7 K/s. Fig. 10(b) shows that the hardness value of the SLM component is the smallest at a scanning speed of 1200 mm/s, which is due to the increase in porosity defects under high energy density leading to a decrease in mechanical properties. The hardness value at 2400 mm/s is slightly lower than that at 1800 mm/s, which is because the insufficient laser energy at high scanning speeds results in more incomplete fusion defects, thereby reducing the mechanical properties. Relatively speaking, SLM components obtained at appropriate scanning speeds such as 1800 mm/s have fewer porosity defects and better mechanical properties.

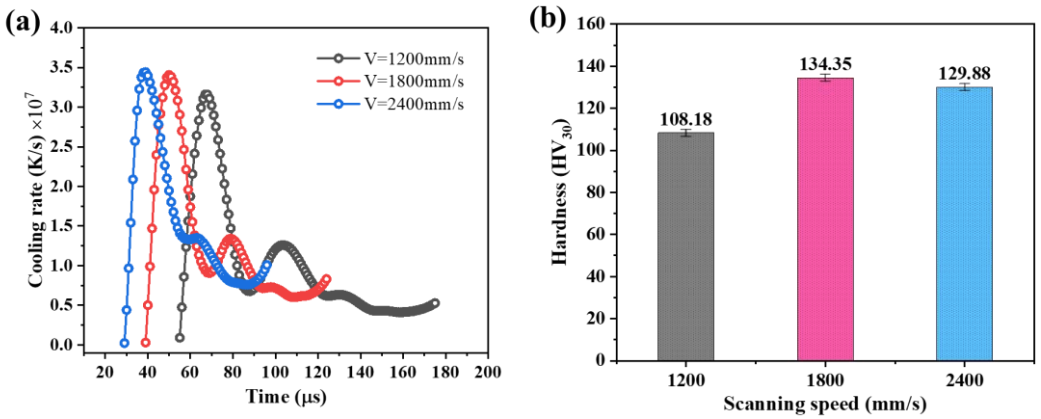

Fig. 10. (a) The average cooling rate of molten pool at different scanning speeds, (b) Vickers hardness of samples at different scanning speeds.

5. Conclusions

Through the establishment of a unified multiphase flow model of gas-liquid-solid phases and combined experimental analysis, the thermodynamic behavior during the selective laser melting (SLM) process has been studied, yielding the following conclusions:

1. The morphology of the melt pool obtained from numerical simulations matches well with experimental results, verifying the reliability of the constructed numerical model. Under high laser energy density, severe keyholes exacerbate the generation of spherical pore defects. Conversely, at low laser energy density, incomplete melting of powder particles leads to the formation of non-spherical pores. Both extreme cases have a negative impact on the SLM components.

2. The evolution of the melt pool is mainly influenced by three driving forces (gasification recoil pressure, Marangoni force, and surface tension). Gasification recoil pressure causes the melt pool surface to indent, and excessive indentation can lead to keyhole formation; Marangoni force promotes the formation of circulating flow in the melt pool; the uneven distribution of surface tension causes periodic oscillations of the melt pool surface.

3. The temperature gradient at the edge of the melt pool is 1.26 E7 K/m, which is 7 times greater than that at the center of the melt pool, which is 1.78 E6 K/m; the solidification rate increases from 0.57 m/s at the edge of the melt pool to 8.34 m/s at the center of the melt pool, an increase of 15 times. A shorter melt pool lifetime (e.g., increasing the scanning speed) is more conducive to optimizing the solidification structure. Therefore, appropriately increasing the scanning speed under suitable laser power is expected to enhance the mechanical properties of SLM components.

Acknowledgment

This research was funded by Foshan Science and Technology Inno-vation Team Project (FS0AA-KJ919-4402-0023), Jihua Laboratory Project (X190061UZ190), Yunfu Industry-University-Research Project (220627155594664), and Guangzhou basic and applied basic research project (202201010393).

References

[1] Debroy, T., et al., Additive manufacturing of metallic components–Process, structure and properties, *Progress in Materials Science*, 92 (2018), pp. 112–224.

[2] Cooper, D. E., et al., Additive layer manufacture of Inconel 625 metal matrix composites, reinforcement material evaluation, *Journal of Materials Processing Technology*, 213 (2013), 12, pp. 2191-2200.

[3] Penchal, M., et al., Microwave Rapid Sintering of Al-Metal Matrix Composites: A Review on the Effect of Reinforcements, Microstructure and Mechanical Properties, *Metals*, 6 (2016), 7, 143.

[4] Salmi, A., et al., An integrated design methodology for components produced by laser powder bed fusion (L-PBF) process, *Virtual and Physical Prototyping*, 13 (2018), 3, pp. 191-202.

[5] Tepylo, N., et al., Laser-Based Additive Manufacturing Technologies for Aerospace Applications, *Advanced Engineering Materials*, 21 (2019), 11.

[6] Chen, H., et al., Flow behavior of powder particles in layering process of selective laser melting: Numerical modeling and experimental verification based on discrete element method, *International Journal of Machine Tools & Manufacture*, 123 (2017), pp. 146-159.

[7] Kovalev, O. B., et al., Theoretical and Experimental Investigation of Gas Flows, Powder Transport and Heating in Coaxial Laser Direct Metal Deposition (DMD) Process, *Journal of Thermal Spray Technology*, 20 (2011), 3, pp. 465-478.

[8] Markl, M., and Koerner, C., Multiscale Modeling of Powder Bed–Based Additive Manufacturing, *Annual Review of Materials Research*, 46 (2016), 1, pp. 93-123.

[9] Thanki, A., et al., Study of keyhole-porosities in selective laser melting using X-ray computed tomography, *9th Conference on Industrial Computed Tomography (iCT)*, 2019.

[10] Lee, K. H. and Yun, G. J., A Novel Heat Source Model for Analysis of Melt Pool Evolution in Selective Laser Melting Process, *Additive Manufacturing*, 36 (2020), 5, 101497.

[11] Li, E. L., et al., A three-phase model for simulation of heat transfer and melt pool behaviour in laser powder bed fusion process, *Powder Technology*, 381 (2020), 4, pp. 298-312.

[12] Dilip, J. J. S., et al., Influence of processing parameters on the evolution of melt pool, porosity, and microstructures in Ti-6Al-4V alloy parts fabricated by selective laser melting, Progress in *Additive Manufacturing*, 2 (2017), 3, pp. 157-167.

[13] Yadroitsev, I., et al., Single track formation in selective laser melting of metal powders, *J.mater.process.technol*, 210 (2010), 12, pp. 1624-1631.

[14] Zuo, D. L., et al., Theoretical studies on free surface morphology of melted pool in laser processing, *Laser Technology*, (1999).
[15] Weirather, J., et al., A Smoothed Particle Hydrodynamics Model for Laser Beam Melting of Ni-based Alloy 718, *Computers & Mathematics with Applications*, 78 (2019), 7, pp. 2377-2394.
[16] Liu, Y., et al., Numerical and experimental investigation into the subsequent thermal cycling during selective laser melting of multi-layer 316L stainless steel, *Optics & Laser Technology*, 98 (2018), pp. 23-32.
[17] Scharowsky, T., et al., Melt pool dynamics during selective electron beam melting, *Applied Physics A*, 114 (2014), 4, pp. 1303-1307.
[18] Bruna-Rosso, C., et al., Selective Laser Melting Finite Element Modeling: Validation with High-Speed Imaging and Lack of Fusion Defects Prediction, *Materials & Design*, 156 (2018), pp. 143-153.
[19] Tseng, C. C., and Li, C. J., Numerical investigation of interfacial dynamics for the melt pool of Ti-6Al-4V powders under a selective laser, *International Journal of Heat and Mass Transfer*, 134 (2019), pp. 906-919.
[20] Ki, H., et al., A Numerical Method for Multiphase Incompressible Thermal Flows with Solid–Liquid and Liquid–Vapor Phase Transformations, *Numerical Heat Transfer Part B Fundamentals*, 48 (2005), 2, pp. 125-145.
[21] Bayat, M., et al., Keyhole-induced porosities in Laser-based Powder Bed Fusion (L-PBF) of Ti6Al4V: High-fidelity modelling and experimental validation, *Additive Manufacturing*, 30 (2019), 100835.
[22] Jafari, R., and Okutucu-Özyurt, T., Phase-field modeling of vapor bubble growth in a microchannel, *J. Comput. Multiph. Flows*, 7 (2015), 3, pp. 143–158.
[23] He, P., et al., Elevated temperature mechanical properties of TiCN reinforced AlSi10Mg fabricated by laser powder bed fusion additive manufacturing, Materials Science & Engineering, A. Structural Materials: Properties, Misrostructure and Processing, 811 (2021).
[24] Saghaian, E., et al., Effect of hatch spacing and laser power on microstructure, texture, and thermomechanical properties of laser powder bed fusion (L-PBF) additively manufactured NiTi, *Optics and Laser Technology*, 149 (2022), 107680.
[25] Wei, H. L, et al., Three-dimensional grain growth during multi-layer printing of a nickel-based alloy Inconel 718, *Additive Manufacturing*, 25 (2018), pp. 448-459.

Submitted: 13.5.2024.
Revised: 30.7.2024.
Accepted: 12.8.2024.